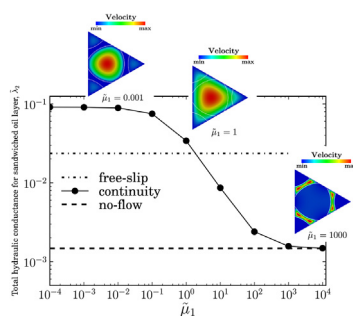Regular Article

A study to investigate viscous coupling effects on the hydraulic conductance of fluid layers in two-phase flow at the pore level

Mosayeb Shams *, Ali Q. Raeini, Martin J. Blunt, Branko Bijeljic

Department of Earth Science and Engineering, Imperial College London, London SW7 2AZ, UK

GRAPHICAL ABSTRACT

ARTICLE INFO

ABSTRACT

This paper examines the role of momentum transfer across fluid-fluid interfaces in two-phase flow. A volume-of-fluid finite-volume numerical method is used to solve the Navier-Stokes equations for two-phase flow at the micro-scale. The model is applied to investigate viscous coupling effects as a function of the viscosity ratio, the wetting phase saturation and the wettability, for different fluid configurations in simple pore geometries. It is shown that viscous coupling effects can be significant for certain pore geometries such as oil layers sandwiched between water in the corner of mixed wettability capillaries. A simple parametric model is then presented to estimate general mobility terms as a function of geometric properties and viscosity ratio. Finally, the model is validated by comparison with the mobilities computed using direct numerical simulation.

1. Introduction

Immiscible two-phase flow through porous media occurs routinely in a wide range of environmental and industrial processes, including enhanced oil recovery [1], carbon dioxide storage in subsurface aquifers [2,3], remediation of contaminated soils [4] and fuel cell technology [5,6].

The macro-scale modelling of these processes requires the specification of macroscopic momentum equations for each of the two fluids. These equations can be conventionally approximated as the extension of Darcy's law to two-phase flow with relative permeabilities for each phase [7]. However, this traditional approach often does not take into account the viscous coupling of the fluids due to the momentum transfer across the fluid-fluid interface [8]. The assumption of uncoupled flows of the fluids can lead to inaccurate results for those two-phase flow regimes in which coupling drag between fluid phases can be significant [9,10].

Several experimental and theoretical studies have reported the significance and effects of viscous coupling in two-phase flows. Whitaker [11] employed a method of volume averaging to analyze immiscible two-phase flow in a general porous medium. He

developed a form of coupled Darcy-like equations containing additional terms that represent the influence of viscous drag exerted between fluid phases. Kalaydjian [12] studied the spontaneous counter-current flow of a non-wetting fluid ganglion by a wetting fluid in a square capillary tube. He proposed a new form of the two-phase Darcy equation in which a matrix of relative permeabilities, with equal off-diagonal terms representing the contribution of the viscous coupling, relates flow rates to pressure gradients. Avraam and Payatakes [13] employed a parameter estimation approach to obtain all four terms of the relative permeability matrix based upon a statistical analysis of experimental data, obtained from a set of steady-state co-current two-phase flows in a micro-model. They disputed the validity of Onsager-Casimir reciprocal relation and found that the off-diagonal coupling coefficients are not necessarily equal. Ehrlich [14] used semi-analytical equations to study the effect of viscous coupling on relative permeabilities in two-phase flow through an idealized model of a porous medium consisting of a bundle of regular polygonal capillary tubes, suggesting that the rheology of the interface can affect the magnitude of viscous coupling.

In addition to empirical and theoretical studies, numerical simulations have been recently used to uncover mechanisms that control and describe viscous coupling effects in two-phase flow at the pore level. Various pore-scale modelling approaches, such as pore-network models [15,16], lattice Boltzman methods [17,18], mesh-free Lagrangian particle methods [19] and Eulerian grid-based methods [20,21], have been employed. Li et al. [22] used a two-phase lattice Boltzmann model for two-phase flow through a homogeneous sphere-pack and systematically studied viscous coupling effects over a broad range of conditions, suggesting fluid-fluid interfacial area as a key parameter which can affect relative permeabilities. Dehghanpour et al. [23] employed a high-resolution finite-element numerical method to investigate viscous coupling for sandwiched layers in angular capillaries in three-phase flow. Xie et al. [24] proposed an improved pore-network model to accommodate viscous coupling effects and examined its efficiency through computing relative permeabilities for some mixed- and water-wet rock samples and provided comparisons with experimental results.

Among pore-scale modelling methods, pore-network models have grown in popularity due to their computational efficiency, which enables them to study large realistic rock samples [25–29]. These models rely upon a simplified representation of the pore space geometry and empirical models for hydraulic conductance and capillary entry pressure in pore/throat elements. The hydraulic conductance for each phase is a key parameter in pore-network models to relate the flow rate of a phase to pressure gradient.

Several studies have been performed to quantify and establish correlations for hydraulic conductances by relating them to pore geometry, contact angle and interface rheology. Ransohoff and Radke [30] employed a finite-element method to model the flow of a wetting phase along corners of predominantly gas-occupied noncircular capillaries. They quantified the relationship between the average velocity of the wetting phase in a corner, $\bar{u}$, and the pressure gradient within the phase, ∇p, as a dimensionless flow resistance, β,

$$\beta = -\frac{R_l^2}{\mu \bar{u}} \nabla p, \tag{1}$$

where R_l is the radius of interface curvature. They reported the computed dimensionless flow resistance for different pore geometries, contact angles and interfacial shear viscosities. Zhou et al. [31] established approximate analytical solutions to relate the dimensionless flow resistance, β, to pore and interface geometry for oil flow along sandwiched layers and water flow along corners of

predominantly gas-occupied noncircular capillaries. Futaisi and Patzek [32] employed a high-resolution finite-element method in conjunction with a projection-pursuit regression approach to determine analytical correlations for three-phase hydraulic conductances in angular capillaries. However, none of theses models take into account the existence of viscous coupling between the flowing fluids and simply assume that conductances are independent of viscosity ratio, i.e. uncoupled flow of the fluids.

This assumption may adversely affect the accuracy of pore-network models when used to predict macroscopic flow properties such as relative permeabilities. Therefore, it is important to establish reliable hydraulic conductance correlations that respect the existence of viscous coupling between the two fluids and incorporate them into pore-network models. To do so, one can perform direct numerical simulations on various two-phase fluid configurations in single micro-scale capillaries to calculate generalized mobilities of each fluid, stabilized by capillary forces. Then, this information can be exploited to find mathematical expressions which can be incorporated into two-phase pore-network models in the form of hydraulic conductivities.

In this work, we first solve two-phase flow through square, triangular and star-shaped pore geometries with uniform and nonuniform wettability conditions using a volume-of-fluid finite-volume based numerical method. Then, we employ an approach similar to Dehghanpour et al. [23] to obtain simple parametric scaling models for the hydraulic conductance of centre, layer and corner flows as a function of the geometry and viscosity ratio. Finally, we find appropriate parameters for each model by fitting against general mobilities that are obtained from the numerical simulations.

2. Pore-scale modelling and validation

In this section, we first give a brief description of the direct numerical simulation approach used to model two-phase flow at the pore level. Then, the accuracy of the model in capturing the viscous coupling effects is validated for a square capillary tube for which a semi-analytical solution is available [14].

2.1. Numerical model

The following single set of Navier-Stokes equations is solved to describe an isothermal, incompressible, immiscible flow of two Newtonian fluids:

$$\nabla \cdot \mathbf{u} = 0, \tag{2}$$

$$\frac{\partial(\rho \mathbf{u})}{\partial t} + \nabla \cdot (\rho \mathbf{u}\mathbf{u}) - \nabla \cdot \mathbb{T} = -\nabla p + \mathbf{F} + \mathbf{f}_c, \tag{3}$$

where $\mathbf{u}$ is the velocity vector, $\mathbb{T} = \mu(\nabla \mathbf{u} + (\nabla \mathbf{u})^T)$ is the viscous stress tensor, ρ is the local density, μ is the local dynamic viscosity, p is pressure, $\mathbf{F}$ is any body force and $\mathbf{f}_c$ is the capillary force computed based on a contour-level surface force model; see Shams et al. [21] for more details.

Since the two fluids are modelled as one single-fluid continuum system, the fluid-fluid interface is treated as a discontinuity in fluid properties using an indicator function, α. Therefore, the fluid properties of the system such as density and dynamic viscosity are calculated proportional to the indicator function,

$$\begin{aligned} \rho &= \alpha \rho_1 + (1 - \alpha)\rho_2, \\ \mu &= \alpha \mu_1 + (1 - \alpha)\mu_2, \end{aligned} \tag{4}$$

where the subscripts 1 and 2 denote the first and second phases, respectively. The indicator function, α, represents the volume fraction of one of the fluids in each computational cell. If the cell is

completely occupied by the first fluid then α is equal to one, and if it is completely occupied by the second fluid then $\alpha = 0$. For the cells that contain the fluid-fluid interface, the value of α is between zero and one.

The interface is algebraically advected through the domain as,

$$\frac{\partial \alpha}{\partial t} + \nabla \cdot (\alpha \mathbf{u}) = 0. \tag{5}$$

The numerical method is implemented based upon a volume-of-fluid finite-volume solver in the OpenFOAM library [33]. Eqs. (2), (3) are coupled using the pressure implicit with splitting of operator (PISO) method of Issa [34] and solved iteratively alongside Eq. (5) to obtain cell-centred velocity and pressure fields. The details of the numerical method, including the validation process, can be found in Shams et al. [21].

2.2. Viscous coupling validation

Here, we validate the accuracy of the numerical model to compute the momentum transfer across the interface due to viscous coupling. Representing the interface as a discontinuity in fluid properties makes it possible to capture the viscous coupling implicitly rather than imposing kinematic and dynamic boundary conditions at prescribed interfaces. We simulate immiscible co-current two-phase flow through a three-dimensional square tube where a non-wetting phase, fluid 2, flows in the centre of the tube while the wetting-phase, fluid 1, moves along the corners of the capillary (see Fig. 1). Simulations are performed for three viscosity ratios with different mesh resolutions. Computed velocity fields are then compared against the semi-analytical solution given by Ehrlich [14].

The flow domain is a cubic square of side $L = 20$ μm, predominantly filled with fluid 2 while fluid 1 resides in the corners. The volumetric saturation of the wetting fluid is $S_1 = 0.2146$. The computational mesh is uniform Cartesian, equal grid spacing $\delta x = \delta y = \delta z = h$, with mesh resolutions of $L/h = 12, 24, 48$, and 72. We apply no-slip boundary conditions on the solid walls with a constant contact angle of zero measured through the wetting phase. Periodic boundary conditions are applied in the flow direction along the z-axis. The dynamic viscosity ratios, $M = \mu_1/\mu_2$, are chosen to be 0.1 ($\mu_1 = 0.1\mu_2 = 10^{-3}$ Pa s), 1 ($\mu_1 = \mu_2 = 10^{-3}$ Pa s), and 10 ($\mu_1 = 10\mu_2 = 10^{-2}$ Pa s); the density ratio is 1 with $\rho_1 = \rho_2 = 1000$ kg/m³. The interfacial tension is $\sigma = 0.03$ N/m and no interfacial shear viscosity at the fluid-fluid interface is considered. Constant body forces, $|\mathbf{F}_1| = |\mathbf{F}_2| = 10$ Pa/m, are imposed,

along the z-axis, for both fluids to reach a steady-state flow through the tube.

Fig. 2 compares the steady-state profiles of simulated axial velocity against the semi-analytical solution, along the diagonal of the square capillary tube, r, for various mesh resolutions and viscosity ratios. For $M = 1$, there is a good agreement between the numerical and the theoretical solutions even for a mesh resolution as low as $L/h = 12$. However, for $M = 0.1$ and $M = 10$, to obtain a velocity field in agreement with the semi-analytical solution, we require higher mesh resolutions to resolve the discontinuity of the fluid properties at the fluid-fluid interface accurately.

For a better comparison, we define the normalized error of the velocity field in a cross-section perpendicular to the flow, $x - y$ cross-section, by

$$E(u_z) = \frac{\sum |u_z - u_z^*|}{\sum u_z^*}, \tag{6}$$

where u_z and u_z^* are, respectively, the numerical and semi-analytical values of velocity normal to the $x - y$ cross-section, and the summation is performed over all the faces of the cross-section.

Fig. 3 plots the error versus mesh resolution for different viscosity ratios. According to this plot, the numerical method exhibits a second-order convergence rate when $M = 1$. However, for the viscosity ratios other than 1, $M = 0.1$ and $M = 10$, the convergence rate decreases. Therefore, to perform accurate simulations for varying viscosity ratios, the mesh resolution is chosen to be $L/h = 72$ for the rest of this study.

3. Geometry configurations and coupled flow modelling

In this section, we first describe pore geometries and related fluid configurations for which viscous coupling effects are investigated. Then, the impact of different interface boundary conditions on the computed hydraulic conductance for these fluid configurations is discussed. Finally, we present our approach to model the coupled flow of two phases by defining a generalized matrix of mobilities similar to the generalized Darcy equation.

Three pore geometries: square, equilateral triangular and star-shaped capillary tubes, with the same inscribed radius of $b = 10$ μm, and different wall lengths, l_w, are considered (see Fig. 4). For each geometry, we set up two fluid configurations: (a) corner flow through pores with uniform wettability as schematically depicted in Fig. 4(a–c), and (b) sandwiched layer flow through pores with nonuniform wettability as shown in Fig. 4(d–f); with the grey region representing fluid 1 (water), and the white region
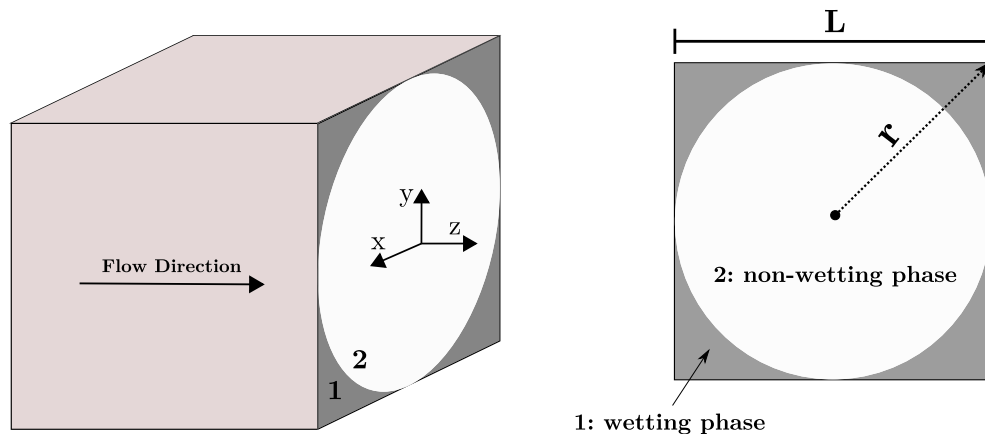

Fig. 1. Schematic illustration of steady-state co-current two-phase flow in a square capillary tube and cross-sectional configuration of the wetting phase, fluid 1, and the non-wetting phase, fluid 2.
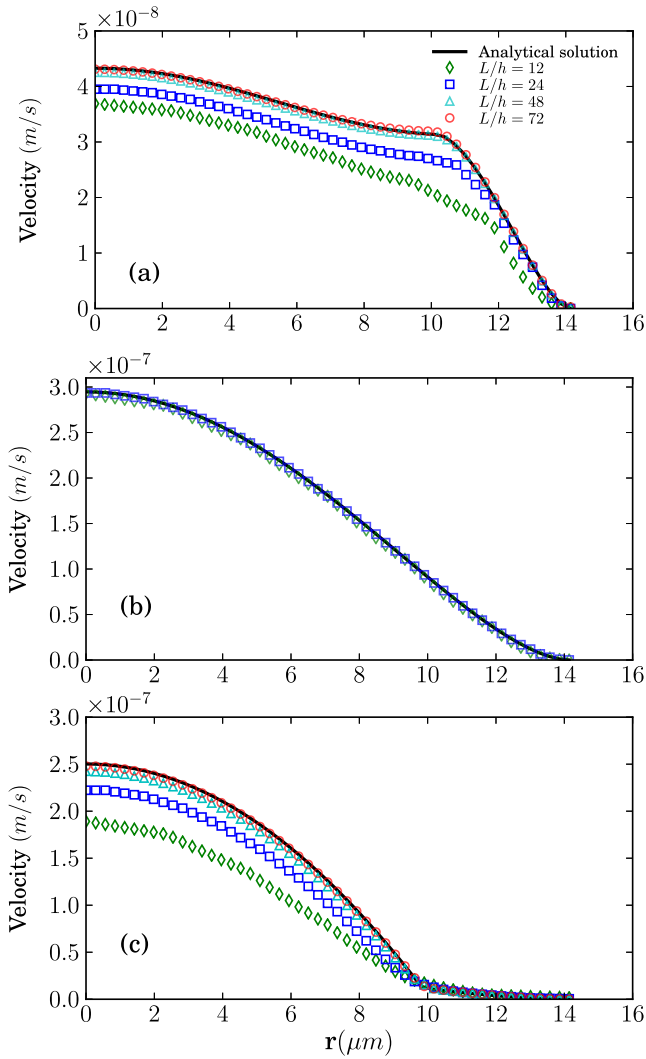
Fig. 2. Axial velocity profiles for co-current two-phase flow along the diagonal of a square capillary tube as a function of mesh resolution in comparison to the semi-analytical solution for viscosity ratios, $M = \mu_1/\mu_2$ of (a) $M = 0.1$, (b) $M = 1$, and (c) $M = 10$.
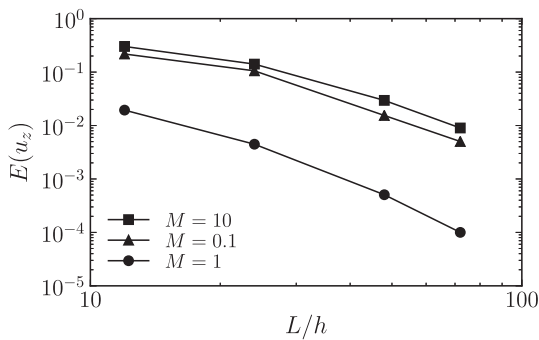

Fig. 3. The normalized error of the computed velocity profile, $E(u_z)$, Eq. (6), versus mesh resolution for two-phase flow with different viscosity ratios, M, in a square capillary tube.

representing fluid 2 (oil). In all cases, flow is perpendicular to the cross-section and driven by a uniform body force.

Fig. 5 depicts the parameters that control the geometry of corner and sandwiched layers in the crevices of the non-circular
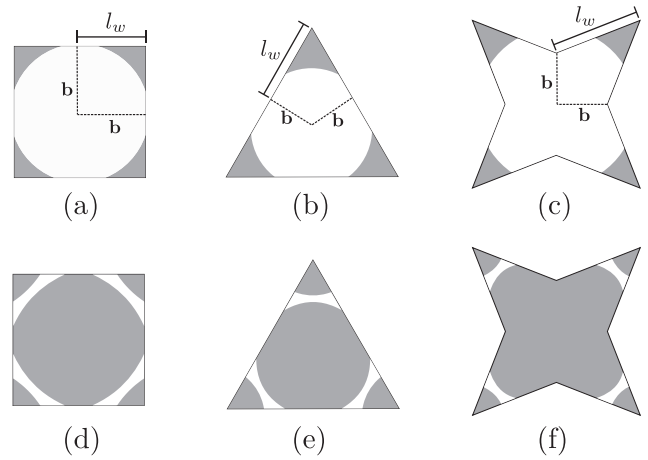

Fig. 4. Schematic illustrations of fluid configurations for square, equilateral triangular and star-shape pore geometries with (a)–(c) uniform wettability, and (d)–(f) nonuniform wettability conditions. For uniform wettability conditions, fluid flow occurs in the corner (grey) and centre (white) of the capillaries, while for nonuniform wettability conditions, in addition to corner and centre flow (grey), we can also have fluid flow in a stabilized intermediate layer (white) sandwiched between the corner and centre of the capillaries. The geometries have different wall lengths, l_w, while the inscribed radius, b, is the same for all geometries and equal to 10 μm.
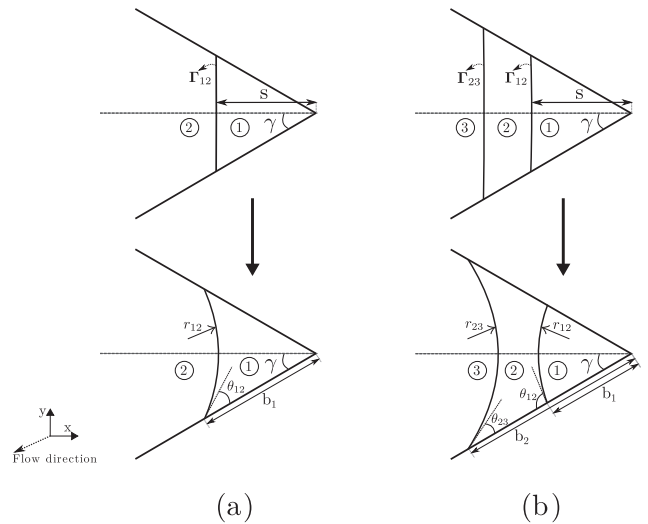

Fig. 5. Schematic illustrations of initial and stabilized form of fluid-fluid interfaces and corresponding geometric parameters for capillaries with (a) uniform wettability conditions, and (b) nonuniform wettability conditions. The curvatures on each side of the sandwiched layer for nonuniform wettability conditions are equal, $r_{12} = r_{23}$.

capillary tubes. For the pores with uniform wetability, in each corner, there is one fluid-fluid interface, Γ_{12}, separating the corner flow of fluid 1 from the centre flow of fluid 2. The geometry of the two fluids can be defined by the corner half-angle (γ), the contact angle (θ_{12}) and the meniscus-apex distance (b_1). For the mixed-wet corners, the shape of sandwiched layers, however, depends on two fluid-fluid interfaces, Γ_{12} and Γ_{23}, which separate the creeping flow of fluid 2 in the intermediate layer from the flow of fluid 1 in the corner and the centre, regions 1 and 3. Therefore, in addition to γ, θ_{12}, and b_1, we also need the meniscus-apex distance and contact angle associated to the Γ_{23} interface, b_2 and θ_{23}, respectively, to define the geometry of the layer [32]. The meniscus-apex distances can be expressed as

$$b_1 = r_{12} \frac{\cos(\theta_{12} + \gamma)}{\sin(\gamma)}, \ b_2 = r_{23} \frac{\cos(\theta_{23} + \gamma)}{\sin(\gamma)}, \tag{7}$$

where r_{12} and r_{23} are, respectively, the radii of curvature of Γ_{12} and Γ_{23}. The contact angle θ_{23} is a free parameter in our simulations, while the contact angle θ_{12} is a hinging value to make the interfacial curvature on both sides of the layer equal, $r_{12} = r_{23}$; see Fig. 5(b).

For each simulation, first, interfaces are initialized as straight lines in each corner, while the parameters, the distance between Γ_{12} centre and the vertex of the corner, is used to control the saturation of fluids in the corner (see Fig. 5). The interfaces are then numerically stabilized for the imposed corner half-angle and contact angle.

We employ the inscribed radius, b, as the characteristic length to scale spatial coordinates, and the viscosity and pressure gradient of fluid 2 (μ_2 and ϕ_2) to scale the velocity of fluids in each flow region [32,23]. The scaling leads to the following dimensionless relations:

$$\tilde{b}_1 = \frac{b_1}{b}, \ \tilde{b}_2 = \frac{b_2}{b}, \ \tilde{l}_w = \frac{l_w}{b},$$
$$\tilde{A}_i = \frac{A_i}{b^2}, \ \tilde{\mu}_i = \frac{\mu_i}{\mu_2}, \ \tilde{\phi}_i = \frac{\phi_i}{\phi_2}, \tag{8}$$
$$\tilde{u}_i = \frac{u_i \mu_2}{\phi_2 b^2},$$

where the subscript i denotes the flow regions in the domain, see Fig. 5, A_i is the area open to flow, and u_i and ϕ_i are the velocity field and pressure gradient in each region. The dimensionless volumetric flow rate passing through region i, Ω_i, is obtained as

$$\tilde{q}_i = \int_{\Omega_i} \tilde{u}_i d\tilde{A}_i. \tag{9}$$

The flow coupling can be influenced by the type of imposed boundary conditions on fluid-fluid interfaces (Γ_{12}, Γ_{23}). Three different boundary conditions can be considered [32]:

1. No-flow boundary condition: the interface is treated as a solid boundary and the velocity of each fluid at the interface is forced to be zero.
2. Free-slip boundary condition: the interface is treated as a perfectly lubricated boundary where fluids can slip freely on top of each other.
3. Continuity boundary condition: there is continuity of velocity and shear stress along the interface and fluids exchange momentum at the interface.

In this work, we employ a direct numerical simulation technique, described in Section 2, to simulate coupled two-phase flow through the capillary tubes. In the numerical method, since the interface is treated as a discontinuity in fluid properties, we do not need to explicitly impose boundary conditions on the interface. Velocity and stress continuity conditions are implicitly captured, i.e. we have the continuity boundary condition along the interface.

We first obtain volumetric fluxes for different flow regions in the capillary tube. Then, the following algebraic equation system is formed based on the generalized Darcy's equation [12,13,8] and solved to compute the flow conductance matrix, $[\tilde{\lambda}_{ij}]$:

$$[\tilde{q}] = -[\tilde{\lambda}_{ij}][\tilde{\phi}], \tag{10}$$

where $[\tilde{q}]$ and $[\tilde{\phi}]$ are the column vectors of the dimensionless volumetric flux and dimensionless pressure gradient for each phase, respectively, and $[\tilde{\lambda}_{ij}]$ is the square matrix of generalized dimensionless mobilities with the off-diagonal terms representing the viscous coupling exerted between fluid phases [12]. The matrix of mobilities is 2 by 2 for uniform wettability configurations,

$$[\tilde{\lambda}_{ij}] = \begin{bmatrix} \tilde{\lambda}_{11} & \tilde{\lambda}_{12} \\ \tilde{\lambda}_{21} & \tilde{\lambda}_{22} \end{bmatrix}, \tag{11}$$

and 3 by 3 for nonuniform wettability configurations,

$$[\tilde{\lambda}_{ij}] = \begin{bmatrix} \tilde{\lambda}_{11} & \tilde{\lambda}_{12} & \tilde{\lambda}_{13} \\ \tilde{\lambda}_{21} & \tilde{\lambda}_{22} & \tilde{\lambda}_{23} \\ \tilde{\lambda}_{31} & \tilde{\lambda}_{32} & \tilde{\lambda}_{33} \end{bmatrix}. \tag{12}$$

The coefficients of the matrix depend on the contact angle, θ, the corner half-angle, γ, the saturation, S, and the viscosity ratio, $\tilde{\mu}$, of the fluids flowing through the capillary. For each fluid configuration and viscosity ratio, to quantify the coefficients, we apply a non-zero pressure gradient to one flow region (centre, layer or corner) and zero pressure gradient to other flow region(s) and solve Eq. (10) based on the resultant volumetric flux vector. This is repeated for all flow regions in the cross-section, two simulations for uniform wettability configurations and three simulations for nonuniform wettability configurations, to obtain all diagonal and off-diagonal terms of the matrix. From our numerical simulations, we observe that the matrix is symmetrical ($\tilde{\lambda}_{12} = \tilde{\lambda}_{21}$, $\tilde{\lambda}_{23} = \tilde{\lambda}_{32}$ and $\tilde{\lambda}_{13} = \tilde{\lambda}_{31}$) which is consistent with Onsager's reciprocity equations [35].

To show the dependence of the velocity profile and consequently flow conductivity on viscosity ratio and interface boundary condition, we model two-phase flow through the equilateral triangular capillary tube with sandwiched layers. Fig. 6 shows the
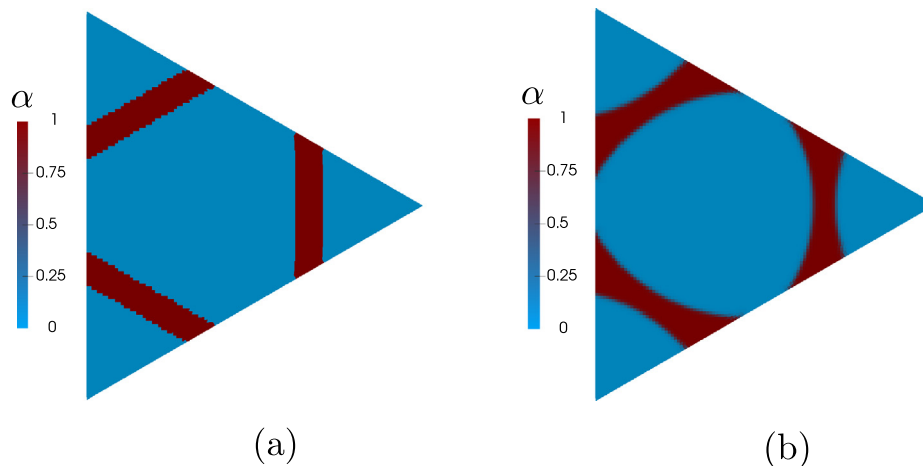
Fig. 6. Visualizations of (a) the initialized, and (b) equilibrium configuration of sandwiched oil layers, $\alpha = 1$, in the corners of an equilateral triangular capillary with $\gamma = \theta_{23} = 30°$, and $S_2 = 0.2$.
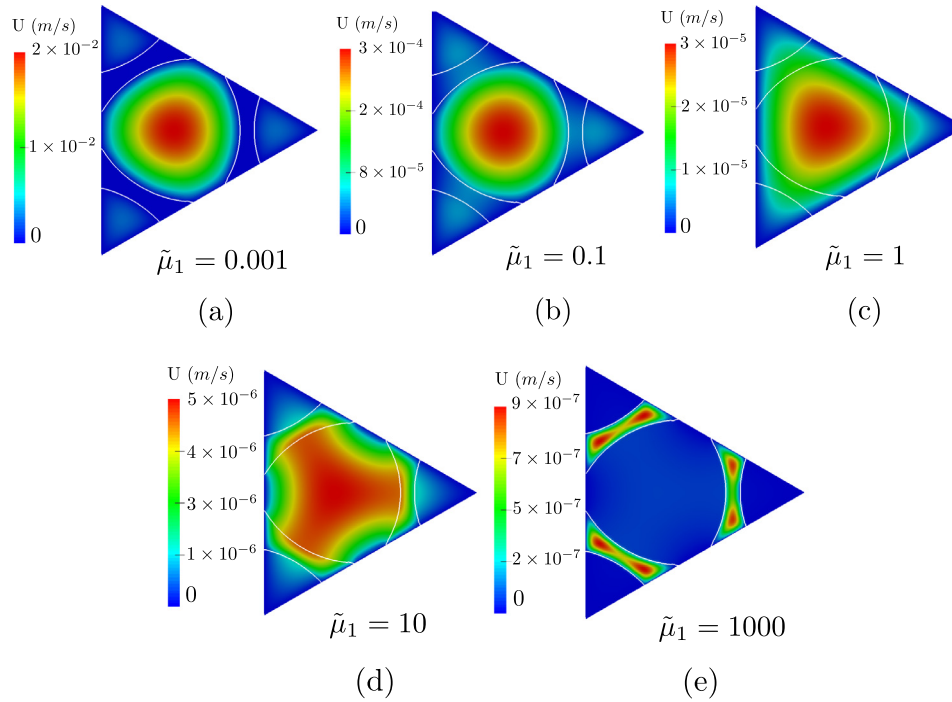
Fig. 7. Steady-state velocity distribution across flowing fluids with different viscosity ratios in an equilateral triangular capillary with $\gamma = \theta_{23} = 30°$, and $S_2 = 0.2$.

initialized and equilibrium configuration of the oil layers for a saturation of $S_2 = 0.2$. The viscosity of the sandwiched oil layers is kept constant and equal to $\mu_2 = 10^{-3}$ Pa s, while the viscosity of water flowing in the corners and centre, μ_1, is changed to have viscosity ratios, $\tilde{\mu}_1 = \mu_1/\mu_2$, ranging from 10^{-4} to 10^4. A uniform pressure gradient (body force) of $\phi_1 = \phi_2 = \phi_3 = 100$ Pa/m is applied perpendicular to the cross-section of the capillary tube. The contact angle is chosen to be $\theta_{23} = 30°$, the interfacial tension is $\sigma = 0.03$ N/m and the continuity of velocity and shear stress is assumed at the interface with zero interfacial shear viscosity.

Fig. 7 compares the steady-state velocity profiles for five sample viscosity ratios. It can be observed that the influence of the viscosity ratio on the value and profile of velocity can be quite significant. When $\tilde{\mu}_1 = 1$, the resultant velocity profile is equivalent to the single-phase flow solution for the domain. As the viscosity ratio deviates from one ($\tilde{\mu}_1 = 0.1$ and $\tilde{\mu}_1 = 10$), the flow coupling between the centre and corner regions decreases. Our simulations show that for very low or high viscosity ratios such as $\tilde{\mu}_1 = 0.001$ and $\tilde{\mu}_1 = 1000$, the flow regions become effectively decoupled from each other. When $\tilde{\mu}_1 = 1000$ the fluid-fluid interface behaves as a solid wall for the sandwiched oil layers, whereas it acts as perfectly lubricated for the water flowing in the centre and corners. The reverse pattern can be observed when $\tilde{\mu}_1 = 0.001$.

Fig. 8 depicts the computed dimensionless total hydraulic conductance,

$$\tilde{\lambda}_i = -\tilde{q}_i/\tilde{\phi}_i, \tag{13}$$

for one of the oil layers, $i = 2$, as a function of viscosity ratio, and compares the results for different interface boundary conditions (free-slip, no-flow, and continuity). It is clear that no-flow and free-slip boundary conditions result in an uncoupled flow of fluids, independent of the viscosity ratio. On the other hand, the computed hydraulic conductance with the continuity boundary condition exhibits a strong dependency on the viscosity ratio. For very high viscosity ratios ($\tilde{\mu}_1 \geqslant 10^3$) the continuity boundary condition behaves similar to the no-flow one, due to the fact that the water

phase in the centre and corners of the capillary has relatively high viscosity values and acts as a solid phase with respect to the oil layers. For very low viscosity ratios ($\tilde{\mu}_1 \leqslant 10^{-2}$) the conductance reaches a maximum at a value higher than the free-slip limit. Exceeding the no-slip limit is a clear indication of the importance of viscous coupling when the water phase drags the intermediate layer along and contributes to its conductance. Therefore, it is important to investigate the viscous coupling effect on the computed transport properties by considering continuity of velocity and shear stress along the interface.

To quantify the contribution of momentum transfer due to viscous coupling, we evaluate the hydraulic conductance matrix, Eq. (12), for different viscosity ratios. Fig. 9 compares the portion of the total hydraulic conductance resulting from the pressure gradient within the sandwiched oil layer, $\tilde{\lambda}_{22}$, to the portions due to the drag force from the adjacent water phase flowing in the centre, $\tilde{\lambda}_{23}$, and corner, $\tilde{\lambda}_{21}$. It can be observed that for viscosity ratios less than
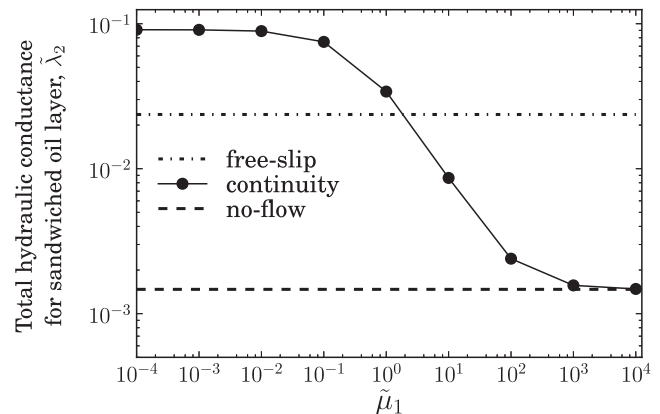

Fig. 8. Dimensionless total hydraulic conductance of a sandwiched oil layer, $\tilde{\lambda}_2$, as a function of viscosity ratio, for different interface boundary conditions. The capillary tube is an equilateral triangle with $\gamma = \theta_{23} = 30°$ and $S_2 = 0.2$.
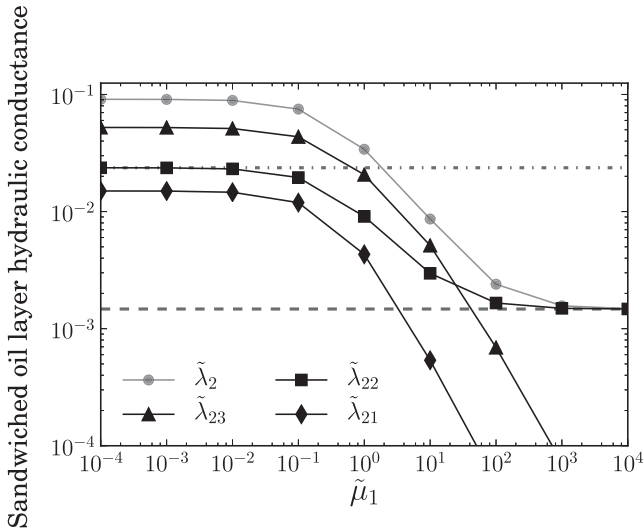
Fig. 9. Comparison of contributing components to the total conductance of a sandwiched oil layer, $\tilde{\lambda}_2$, in a triangular capillary tube with $\gamma = \theta_{23} = 30°$ and $S_2 = 0.2$: the conductance resulting from the pressure gradient within the oil phase in layer, $\tilde{\lambda}_{22}$, and the conductance due to the drag force exerted from the neighbouring water phase in the centre $\tilde{\lambda}_{23}$, and corner $\tilde{\lambda}_{21}$.

Fig. 10. Comparisons of the dimensionless resistance, β, Eq. (1), for wetting phase flow along the sharp corners of a square capillary tube, as a function of contact angle, θ_{12}. The wetting phase in corners, fluid 1, is driven by a constant nonzero pressure gradient, while the pressure gradient within the non-wetting phase in the centre, fluid 2, is zero: (a) $\tilde{\mu}_1 = \mu_1/\mu_2 \leqslant 1$, (b) $\tilde{\mu}_1 = \mu_1/\mu_2 > 1$.

0.1, the values of $\tilde{\lambda}_{23}$ become higher than $\tilde{\lambda}_{22}$, which indicates the importance of the momentum transfer across the interface between the centre and the oil layer, and also justifies the exceeding of the total conductance, $\tilde{\lambda}_2 = \tilde{\lambda}_{21} + \tilde{\lambda}_{22} + \tilde{\lambda}_{23}$, from the free-slip limit.

To further investigate this, we model two-phase flow through a square capillary tube with uniform wettability, Fig. 4(a). The dimensionless flow resistance, β, Eq. (1), for the wetting liquid along one of the corners is computed for different contact angles and viscosity ratios. The results are compared with the study of Ransohoff and Radke [30] when the comparison is possible, i.e. wetting phase flow in sharp corners while the interfacial shear viscosity, μ_s, is either zero (equivalent to the free-slip boundary condition) or infinite (equivalent to the no-flow boundary condition).

First, we consider a flow arrangement in which the wetting phase, fluid 1, flow in corners is driven by a constant non-zero pressure gradient while the pressure gradient within the central non-wetting phase, fluid 2, is zero. This means that the stress exerted by the non-wetting phase, due to its flow in the centre, on the interface is zero, which is in accordance with the assumption of having an inviscid central phase in Ransohoff and Radke [30]. We keep the viscosity of the wetting phase constant, $\mu_1 = 10^{-3}$ Pa s, and decrease or increase the viscosity of the non-wetting phase in the centre, μ_2, to set different viscosity ratios, $\tilde{\mu}_1 = \mu_1/\mu_2$. Fig. 10 shows the computed dimensionless flow resistance as a function of contact angle for a large range of viscosity ratios. For $\tilde{\mu}_1 = 1$ and $\tilde{\mu}_1 = 0.1$ the dimensionless resistances are overestimated when assuming a no-flow boundary condition [30] and this assumption can be a good approximation only when the viscosity of the central phase is very high compared to the wetting phase in the corners, $\tilde{\mu}_1 \leqslant 10^{-2}$. On the other hand, the free-slip boundary condition can be a very good approximation for viscosity ratios more than one, as shown in Fig. 10(b). This is expected due to the fact that the non-wetting phase in the centre is relatively less viscous and since the pressure gradient within this phase is zero the drag force exerted on the interface is insignificant.

Finally, we perform a similar analysis for the case that both fluids are driven using an identical non-zero pressure gradient in a co-current flow. Fig. 11(a) demonstrates that the solution beha-
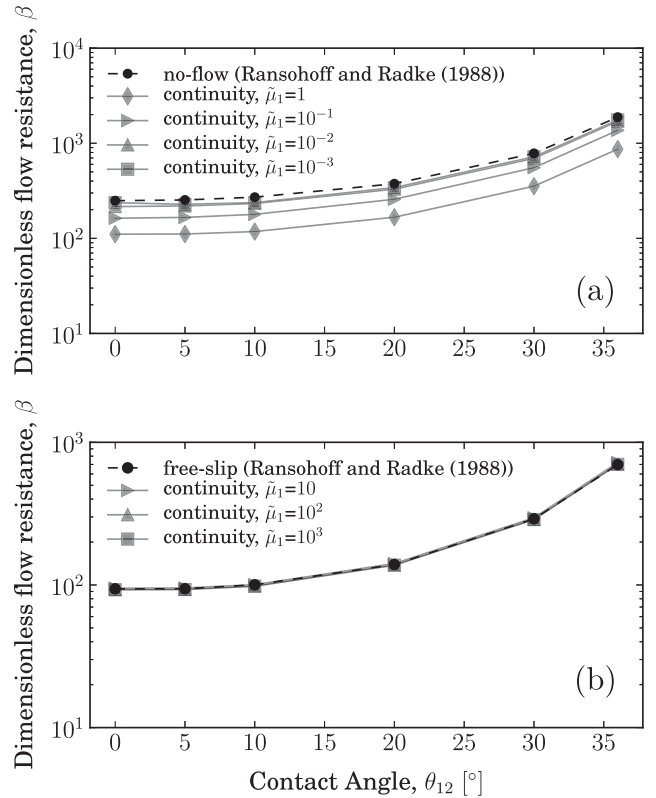
viour for $\tilde{\mu}_1 \leqslant 1$ is quite similar to the previous case, Fig. 10(a). However, as shown in Fig. 11(b), for $\tilde{\mu}_1 > 1$, the numerical results of Ransohoff and Radke [30], with a free-slip boundary at the interface, significantly overestimates the dimensionless resistances. This can be explained by the fact that the non-wetting phase with a low viscosity can move at a relatively high velocity, which results in a significant drag force on the interface that enhances the flow conductance of the wetting phase in the corners.

These results highlight the importance of momentum transfer across the interface, especially for mid-range viscosity ratios, $10^{-2} \leqslant \tilde{\mu}_1 \leqslant 10^2$, where treating the coupled two-phase flow problem as independent flows of fluids separated by no-flow or free-slip interfacial boundaries can introduce significant errors in the computation of hydraulic conductance. In the next section, we propose and validate some simple relations to estimate hydraulic conductances which take into account the viscous coupling effects due to momentum exchange at the interface.

4. Scaling models and validation

In this section, we provide heuristic models to relate the generalized mobilities ($\tilde{\lambda}_{ij}$) to the geometrical parameters (γ, θ_{12}, θ_{23}) and viscosity ratio ($\tilde{\mu}$). These generalized mobilities are then compared with the corresponding numerical solutions and the average of relative absolute errors are reported. Dehghanpour et al. [23] also developed an empirical model to estimate the generalized mobilities for wetting layers (water) and intermediate layers (oil) in three-phase flow through angular capillaries, assuming the central fluid (gas) is decoupled and does not exchange momentum with the oil and water. We follow a similar argument to develop expressions to estimate the generalized mobilities in two-phase
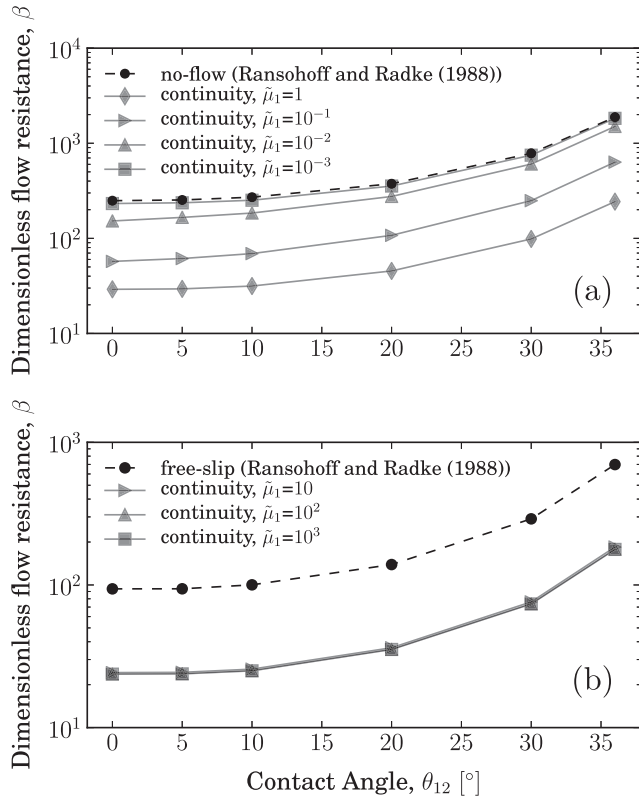
Fig. 11. Comparisons of the dimensionless resistance, β, Eq. (1), for wetting phase flow along the sharp corners of a square capillary tube, as a function of contact angle, θ_{12}. The wetting phase in corners, fluid 1, and the non-wetting phase, fluid 2, in the centre are driven by a constant nonzero pressure gradient, i.e. co-current flow: (a) $\tilde{\mu}_1 = \mu_1/\mu_2 \leqslant 1$, (b) $\tilde{\mu}_1 = \mu_1/\mu_2 > 1$.

flow for (a) uniform wettability where oil in the centre exchanges momentum with water in the corners of a capillary, and (b) nonuniform wettability conditions where there is flow coupling between oil in the sandwiched layers and water in the centre and corners of a capillary.

4.1. Conventional (diagonal) terms

For laminar fully-developed pressure-driven single-phase flow through a straight duct with a constant cross-section, the volumetric flow rate, $\tilde{q}$, can be related to the fluid pressure drop, $\tilde{\phi}$, as follows [23]:

$$\tilde{q} = \tilde{\lambda}\tilde{\phi}, \tag{14}$$

where

$$\tilde{\lambda} = \frac{c}{\tilde{\mu}} \frac{\left(\tilde{A}\right)^3}{\left(\tilde{p}_w\right)^2}. \tag{15}$$

Here c is a proportionality constant which depends only on the duct shape, $\tilde{A}$ is the open area to flow, and $\tilde{p}_w$ is the wetted perimeter defined as the length along which the fluid is in contact with solid

walls where the velocity is zero. Since the diagonal terms of the matrix of mobilities represent the uncoupled pressure-driven flow of each fluid under its own pressure gradient through a duct-shaped passage, in analogy with Eq. (15), the following parametric equation is employed to estimate the diagonal mobilities:

$$\tilde{\lambda}_{ii} = \frac{c_i}{\tilde{\mu}_i} \frac{\left(\tilde{A}_i\right)^{a_i+2}}{\left(\tilde{p}_{w,i}\right)^{2a_i}}, \; i = 1, 2, 3 \tag{16}$$

where the subscript i denotes the flow region, and c_i and a_i are constant parameters for the flow region i.

In two-phase flow, the wetted perimeter of the flow region, $\tilde{p}_{w,i}$, in addition to the fluid–solid boundary, can include the fluid-fluid interface, depending on the viscosity ratio of the adjacent fluids [23]. For the case that the adjacent phase viscosity becomes much higher than the viscosity of the phase in region i, the interface acts as a no-flow boundary for region i and $\tilde{p}_{w,i}$ should include the length of the interface. On the other hand, when the viscosity of the neighbouring phase is much lower than the viscosity of the phase in region i, the adjacent phase is inviscid compared to the phase in region i and $\tilde{p}_{w,i}$ does not include the length of the interface. Therefore, we use the following expressions to relate the wetted perimeter to viscosity ratio for (a) the uniform wettability condition [23],

$$\begin{aligned} \text{corner}: \; &\tilde{p}_{w,1} = 2\tilde{b}_1 + \tilde{l}_{12}f(\tilde{\mu}_1), \\ \text{centre}: \; &\tilde{p}_{w,2} = 2\left(\tilde{l}_w - \tilde{b}_1\right) + \tilde{l}_{12}f\left(\tfrac{1}{\tilde{\mu}_1}\right), \end{aligned} \tag{17}$$

and (b) for the nonuniform wettability condition,

$$\begin{aligned} \text{corner}: \; &\tilde{p}_{w,1} = 2\tilde{b}_1 + \tilde{l}_{12}f(\tilde{\mu}_1), \\ \text{layer}: \; &\tilde{p}_{w,2} = 2\left(\tilde{b}_2 - \tilde{b}_1\right) + \tilde{l}_{12}f\left(\tfrac{1}{\tilde{\mu}_1}\right) + \tilde{l}_{23}f\left(\tfrac{1}{\tilde{\mu}_1}\right), \\ \text{centre}: \; &\tilde{p}_{w,3} = 2\left(\tilde{l}_w - \tilde{b}_2\right) + \tilde{l}_{23}f(\tilde{\mu}_1). \end{aligned} \tag{18}$$

Here $\tilde{l}_{12}$ and $\tilde{l}_{23}$ are, respectively, the dimensionless length of interface Γ_{12} and Γ_{23}, scaled by the inscribed radius, b, and the function f is defined using the following decay function:

$$f(x) = \frac{1}{1 + nx^n}, \tag{19}$$

where the value of $n = 2$ is chosen to fit the simulation data.

The values reported in Table 1 for parameters in Eq. (16) are found to fit our simulations best for uniform and nonuniform wettability conditions.

To validate the scaling model we have simulated two-phase flow through square ($\gamma = 45°$), triangular ($\gamma = 30°$), and star-shaped ($\gamma = 22.5°$) pore geometries, see Fig. 4, for different contact angles ($\theta_{12} = 30°$, $45°$ and $60°$) and volume saturations (S_2). For each case, the coefficients of the matrix of dimensionless mobilities are computed as described in Section 3. Fig. 12 compares the predicted values of the diagonal terms, $\tilde{\lambda}_{11}$, $\tilde{\lambda}_{22}$, and $\tilde{\lambda}_{33}$, using the proposed scaling model, Eq. (16), with the numerically simulated values for uniform and nonuniform wettability cases. The proposed correlation agrees well with the simulated values over four orders of magnitude in conductance.

Table 1
Fitted values for the parameters of Eq. (16), usud to estimate the diagonal terms in the general mobility matrix for uniform and nonuniform wettability configurations.

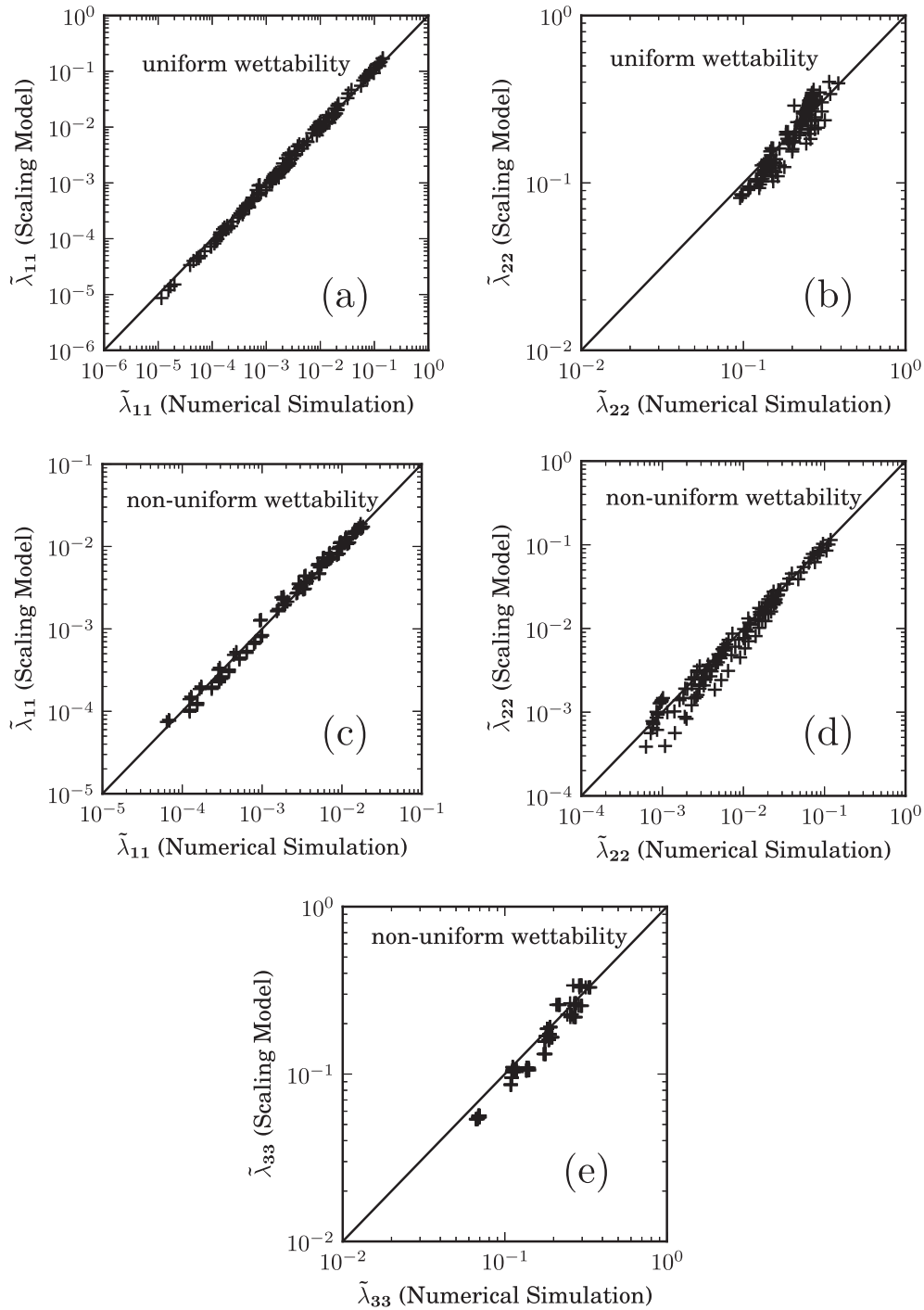|	Uniform	Wetability	Nonuniform wetability		
	$\tilde{\lambda}_{11}$ Corner	$\tilde{\lambda}_{22}$ Centre	$\tilde{\lambda}_{11}$ Corner	$\tilde{\lambda}_{22}$ Layer	$\tilde{\lambda}_{33}$ Centre
c_i	1/7	1/6	1/7	1/3	1/5
a_i	0.45	0.2	0.45	0.75	0.4

Fig. 12. Comparison of the predicted values of the scaling model, Eq. (16), with the simulated values of the diagonal terms. (a)–(b) The diagonal mobilities for corner and centre flow in capillaries with uniform wettability, $\tilde{\lambda}_{11}$ and $\tilde{\lambda}_{22}$, respectively. (c)–(e) The diagonal mobilities for corner, sandwiched layer, and centre flow in capillaries with nonuniform wettability, $\tilde{\lambda}_{11}$, $\tilde{\lambda}_{22}$ and $\tilde{\lambda}_{33}$, respectively.

To quantify the error, we define the mean absolute relative error as follows:

$$\bar{E}\left(\tilde{\lambda}_{ii}\right) = \sum_{N} \left(\frac{|\tilde{\lambda}_{ii}^{num} - \tilde{\lambda}_{ii}^{scale}|}{\tilde{\lambda}_{ii}^{num}} \right)/N, \ i = 1, 2, 3 \qquad (20)$$

where $\tilde{\lambda}_{ii}^{num}$ and $\tilde{\lambda}_{ii}^{scale}$ are the values of the dimensionless mobility computed using numerical simulation and the scaling model, respectively, and $N = 144$ is the total number of fluid configurations which have been simulated. The error values are reported in Table 2.

4.2. Coupling (off-diagonal) terms

The off-diagonal terms of the matrix of mobilities represent the coupled drag-driven flow of each fluid in a flow region resulting from the pressure gradient in the other adjacent flow regions. The simplest type of flow in fluid mechanics similar to this

Table 2
The mean relative errors, Eq. (20), in the predicted diagonal terms using Eq. (16).

| | Uniform | Wetability | Nonuniform wetability | | |
	$\tilde{\lambda}_{11}$	$\tilde{\lambda}_{22}$	$\tilde{\lambda}_{11}$	$\tilde{\lambda}_{22}$	$\tilde{\lambda}_{33}$
$\overline{E}(\tilde{\lambda}_{ii})$	13%	14%	12%	17%	13%

Table 3
Fitted values for the parameters of Eqs. (24) and (25), used to estimate diagonal terms in the general mobility matrix for uniform and nonuniform wettability configurations.

| | Uniform wetability | Nonuniform wetability | | |
	$\tilde{\lambda}_{12}$ Centre-corner	$\tilde{\lambda}_{12}$ Corner-layer	$\tilde{\lambda}_{23}$ Layer-centre	$\tilde{\lambda}_{13}$ Centre-corner
c_{ij}	0.25	0.5	0.4	0.8
a_{ij}	0.5	0.5	0.3	1.1
d_{ij}	γ	γ	1	γ
g	$\frac{2}{2+5\tilde{\mu}_1}$	$\frac{5}{5+4/\tilde{\mu}_1}$	$\frac{1.2}{5+7/\tilde{\mu}_1}$	$\frac{6(1/\tilde{\mu}_1)^2}{\left(0.4\tilde{A}_r+2/\tilde{\mu}_1\right)^{2.5}}$

drag-driven flow in a capillary tube, is Couette flow in which we have a laminar flow in the space between two parallel plates due to a shear stress, τ_s, exerted to one of the plates while the other is fixed [23]. The volumetric flow rate in Couette flow can be related to the shear stress, open area to flow and wetted perimeter in the following dimensionless form [36]:

$$\tilde{q} = \frac{1}{\tilde{\mu}} \frac{\left(\tilde{A}\right)^2}{\tilde{p}_w} \tilde{\tau}_s. \tag{21}$$

In the case of two-phase flow through a capillary, by analogy with Eq. (21), the volumetric flow rate of the fluid in region i due to the drag force resulting from the pressure gradient in the adjacent flow region j, can be estimated as

$$\tilde{q}_i = \frac{c_{ij}}{\tilde{\mu}_i} \frac{\left(\tilde{A}_i\right)^2}{\tilde{p}_{w,i}} \tilde{\tau}_{ij}, \ i \neq j, \tag{22}$$
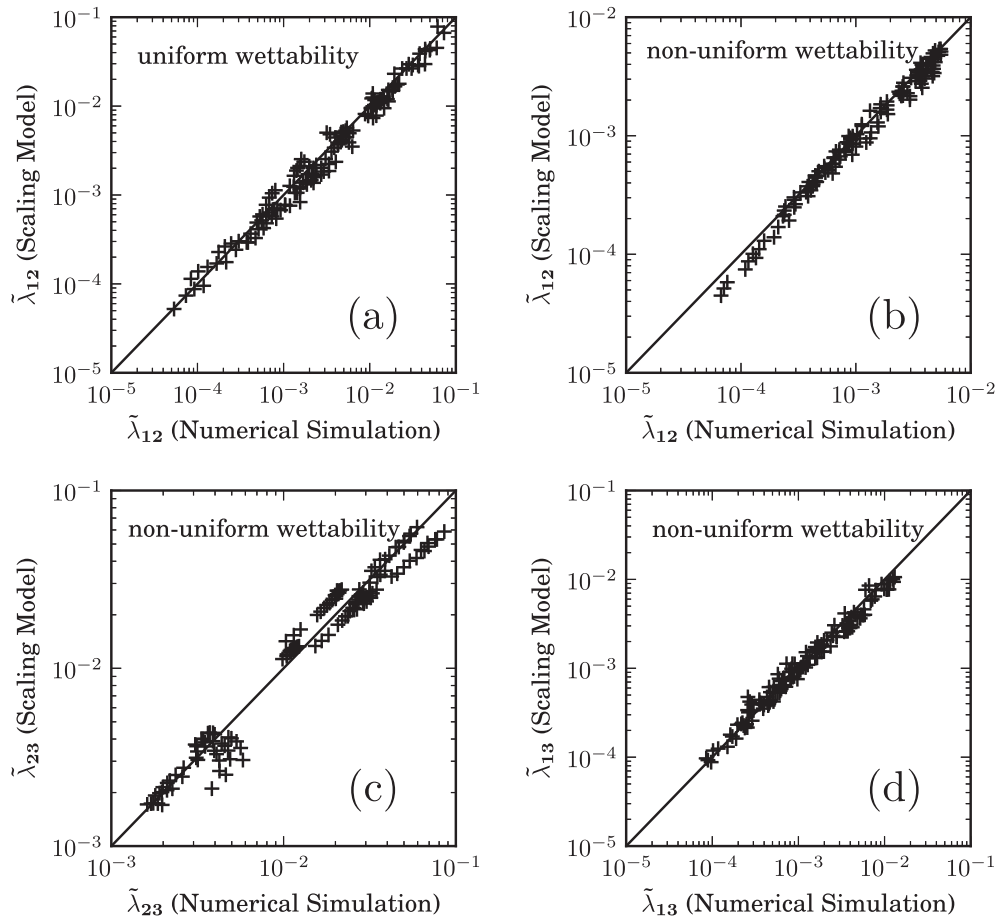

Fig. 13. Comparison of the predicted values of the scaling model, Eqs. (24) and (25), with the simulated values of the coupling terms: (a) the centre-corner coupled mobility term, $\tilde{\lambda}_{12}$, in capillaries with uniform wettability, and (b)–(d) the layer-corner coupled mobility term, $\tilde{\lambda}_{12}$, the layer-centre coupled mobility term, $\tilde{\lambda}_{23}$, and the centre-corner coupled mobility term, $\tilde{\lambda}_{13}$, in capillaries with nonuniform wettability.

Table 4
The mean relative errors, Eq. (20), in predicted coupling terms using Eqs. (24) and (25).

	Uniform wetability	Nonuniform wetability		
	$\tilde{\lambda}_{12}$	$\tilde{\lambda}_{12}$	$\tilde{\lambda}_{23}$	$\tilde{\lambda}_{13}$
$\overline{E}(\tilde{\lambda}_{ij})$	19%	11%	16%	15%

where c_{ij} is a constant parameter, and the shear stress exerted on the fluid–fluid interface, $\tilde{\tau}_{ij}$, can be expressed as a function of flow geometry, viscosity ratio and pressure gradient as follows [23]:

$$\tilde{\tau}_{ij} = g(\tilde{\mu}_1) \frac{\tilde{A}_j}{\tilde{p}_{w,j}} \tilde{\phi}_j, \ i \neq j. \tag{23}$$

Here the function $g(\tilde{\mu}_j)$ is used to relate $\tilde{\tau}_{ij}$ to the viscosity ratio and is estimated by finding the best fit for simulated values of the coupling term as a function of the viscosity ratio.

By substituting Eq. (23) in Eq. (22) and comparing with $\tilde{q}_i = \tilde{\lambda}_{ij}\tilde{\phi}_j$, the following parametric equation can be written for the coupling terms:

$$\tilde{\lambda}_{ij} = c_{ij} \frac{g(\tilde{\mu}_1)}{\tilde{\mu}_i} \frac{\left(\tilde{A}_i\right)^{a_{ij}+1.5} \left(\tilde{A}_j\right)^{d_{ij}+0.5}}{\left(\tilde{p}_{w,i}\right)^{2a_{ij}} \left(\tilde{p}_{w,j}\right)^{2d_{ij}}}, \ i = 1, 2, j = i + 1, \tag{24}$$

where a_{ij} and d_{ij} are constant parameters.

The scaling model for $\tilde{\lambda}_{13}$, however, is computed slightly differently from the one for $\tilde{\lambda}_{12}$ and $\tilde{\lambda}_{23}$, due to the fact that flow regions 1 and 3 are filled with the same fluid separated by an intermediate layer in region 2. Since the shear stress gets transmitted via an intermediate layer, the geometrical parameters of the layer ($\tilde{A}_2$ and $\tilde{p}_{w,2}$) as well as the viscosity ratio can affect $\tilde{\lambda}_{13}$. Therefore, the function g in Eq. (23) is expressed as a function of both viscosity ratio and relative thickness of the intermediate layer. In addition, Eq. (24) is modified to include the momentum dissipation through the wetted perimeter of the intermediate layer:

$$\tilde{\lambda}_{13} = c_{13} \frac{g\left(\tilde{\mu}_1, \tilde{A}_r\right)}{\tilde{\mu}_1} \frac{\left(\tilde{A}_3\right)^{a_{13}+1.5}}{\left(\tilde{p}_{w,2} + \tilde{p}_{w,3}\right)^{2a_{13}}} \frac{\left(\tilde{A}_1\right)^{d_{13}+0.5}}{\left(\tilde{p}_{w,1}\right)^{2d_{13}}}, \tag{25}$$

where $\tilde{p}_{w,1} = 2\tilde{b}_1$, $\tilde{p}_{w,2} = 2\left(\tilde{b}_2 - \tilde{b}_1\right)$, $\tilde{p}_{w,3} = 2\left(\tilde{l}_w - \tilde{b}_2\right)$, and the function $g\left(\tilde{\mu}_1, \tilde{A}_r\right)$ is used to relate the shear stress, $\tilde{\tau}_{13}$, to both viscosity ratio and relative thickness of the intermediate layer, $\tilde{A}_r$, defined as

$$\tilde{A}_r = \left(\frac{\tilde{A}_2}{\tilde{A}_1 + \tilde{A}_3}\right)^{0.5}. \tag{26}$$

The relative thickness $\tilde{A}_r$ controls the momentum dissipation in the intermediate layer. Larger values of $\tilde{A}_r$ means more momentum dissipation through the intermediate layer and consequently, less momentum exchange and viscous coupling between fluids in regions 1 and 3. Therefore the function g should have an inverse relation to $\tilde{A}_r$. Moreover, if $\tilde{\mu}_1 \ll 1$ or $\tilde{\mu}_1 \gg 1$, i.e. the intermediate layer acts as a solid barrier or an inviscid phase, g approaches to zero to decouple the flows in region 1 and 3, $\tilde{\lambda}_{13} = 0$.

Table 3 reports the constant parameters (a_{ij}, c_{ij} and d_{ij}) and function g, used in Eqs. (24) and (25), which are found based on the best fit to the values of $\tilde{\lambda}_{ij}$ computed from our numerical simulations for all geometries.

Fig. 13 compares the predicted values for the coupling terms, $\tilde{\lambda}_{12} = \tilde{\lambda}_{21}$, $\tilde{\lambda}_{23} = \tilde{\lambda}_{32}$, and $\tilde{\lambda}_{13} = \tilde{\lambda}_{31}$, based on the proposed scaling model, Eqs. (24) and (25), with the numerical results, for both uniform and nonuniform wettability cases. One can observe that the scaling model can estimate the coupling mobilities with a good accuracy. The mean relative errors, Eq. (20), for the coupling terms are given in Table 4.

5. Conclusions

In this paper, we have studied viscous coupling effects in two-phase flow through non-circular capillary tubes with uniform and non-uniform wettability conditions. The results indicate that momentum transfer across the interface due to viscous coupling can significantly affect the hydraulic conductance of fluid layers that form in corners of a capillary. We have demonstrated that for clean interfaces where the interfacial shear viscosity is zero, the amount of flow in corners and sandwiched layers using free-slip and no-flow boundary conditions, for a specific range of viscosity ratios, can deviate significantly from those computed using the physically correct continuity boundary condition.

We use two-phase direct numerical simulation results in conjunction with basic arguments from fluid mechanics to present simple hydraulic conductance relations that take into account the viscous coupling effects. These relations, which are validated against numerical results for a wide range of geometric parameters and viscosity ratios, can be incorporated into pore-to-Darcy-scale flow models, for example two-phase pore-network models, to study the effects of viscous coupling on macroscopic flow properties such as relative permeabilities.

References

[1] L.W. Lake, Enhanced Oil Recovery, Prentice Hall, 1989.
[2] L. Marini, Geological Sequestration of Carbon Dioxide: Thermodynamics, Kinetics, and Reaction Path Modeling, Elsevier, 2006.
[3] A. Yamasaki, An overview of CO2 mitigation options for global warming emphasizing CO2 sequestration options, J. Chem. Eng. Japan 36 (4) (2003) 361–375.
[4] C.N. Mulligan, R.N. Yong, B.F. Gibbs, Surfactant-enhanced remediation of contaminated soil: a review, Eng. Geol. 60 (1) (2001) 371–380.
[5] S. Srinivasan, Fuel Cells: From Fundamentals to Applications, Springer Science & Business media, 2006.
[6] W. He, J.S. Yi, T. Van Nguyen, Two-phase flow model of the cathode of PEM fuel cells using interdigitated flow fields, AIChE J. 46 (10) (2000) 2053–2064.
[7] M.J. Blunt, Multiphase Flow in Permeable Media: A Pore-Scale Perspective, Cambridge University Press, 2017.
[8] W. Rose, Myths about later-day extensions of Darcy's law, J. Pet. Sci. Eng. 26 (1) (2000) 187–198.
[9] D.G. Avraam, A.C. Payatakes, Flow regimes and relative permeabilities during steady-state two-phase flow in porous media, J. Fluid Mech. 293 (1995) 207–236.
[10] D.G. Avraam, A.C. Payatakes, Flow mechanisms, relative permeabilities, and coupling effects in steady-state two-phase flow through porous media. The case of strong wettability, Ind. Eng. Chem. Res. 38 (3) (1999) 778–786.
[11] S. Whitaker, Flow in porous media II: The governing equations for immiscible, two-phase flow, Transp. Porous Media 1 (2) (1986) 105–125.
[12] F. Kalaydjian, Origin and quantification of coupling between relative permeabilities for two-phase flows in porous media, Transp. Porous Media 5 (3) (1990) 215–229.
[13] D.G. Avraam, A.C. Payatakes, Generalized relative permeability coefficients during steady-state two-phase flow in porous media, and correlation with the

flow mechanisms, in: Multiph. Flow Porous Media, Springer, 1995, pp. 135–168.

[14] R. Ehrlich, Viscous coupling in two-phase flow in porous media and its effect on relative permeabilities, Transp. Porous Media 11 (3) (1993) 201–218.

[15] I. Fatt, The network model of porous media III. Dynamic properties of networks with tube radius distribution, Trans. AIME 207 (1956) 164–181.

[16] M. Blunt, P. King, Relative permeabilities from two-and three-dimensional pore-scale network modelling, Transp. Porous Media 6 (4) (1991) 407–433.

[17] C. Pan, M. Hilpert, C.T. Miller, Lattice-Boltzmann simulation of two-phase flow in porous media, Water Resour. Res. 40 (1) (2004) W01501.

[18] X. Shan, H. Chen, Lattice Boltzmann model for simulating flows with multiple phases and components, Phys. Rev. E 47 (3) (1993) 1815.

[19] A.M. Tartakovsky, P. Meakin, Pore scale modeling of immiscible and miscible fluid flows using smoothed particle hydrodynamics, Adv. Water Resour. 29 (10) (2006) 1464–1478.

[20] P. Meakin, A.M. Tartakovsky, Modeling and simulation of pore-scale multiphase fluid flow and reactive transport in fractured and porous media, Rev. Geophys. 47 (3).

[21] M. Shams, A.Q. Raeini, M.J. Blunt, B. Bijeljic, A numerical model of two-phase flow at the micro-scale using the volume-of-fluid method, J. Comput. Phys. 357 (2018) 159–182.

[22] H. Li, C. Pan, C.T. Miller, Pore-scale investigation of viscous coupling effects for two-phase flow in porous media, Phys. Rev. E 72 (2) (2005) 26705.

[23] H. Dehghanpour, B. Aminzadeh, D.A. DiCarlo, Hydraulic conductance and viscous coupling of three-phase layers in angular capillaries, Phys. Rev. E 83 (6) (2011) 66320.

[24] C. Xie, A.Q. Raeini, Y. Wang, M.J. Blunt, M. Wang, An improved pore-network model including viscous coupling effects using direct simulation by the lattice Boltzmann method, Adv. Water Resour. 100 (2017) 26–34.

[25] S. Bryant, M.J. Blunt, Prediction of relative permeability in simple porous media, Phys. Rev. A 46 (4) (1992) 2004–2011.

[26] S. Bakke, P.E. Øren, 3-D pore-scale modelling of sandstones and flow simulations in the pore networks, SPE J. 2 (2) (1997) 136–149.

[27] M.J. Blunt, Flow in porous media: pore-network models and multiphase flow, Curr. Opin. Colloid Interface Sci. 6 (3) (2001) 197–207.

[28] P.E. Øren, S. Bakke, Reconstruction of Berea sandstone and pore-scale modelling of wettability effects, J. Pet. Sci. Eng. 39 (3-4) (2003) 177–199.

[29] M.I.J. Van Dijke, K.S. Sorbie, M. Sohrabi, D. Tehrani, A. Danesh, Three-phase flow in WAG processes in mixed-wet porous media: pore-scale network simulations and comparison with micromodel experiments, SPE J. 9 (01) (2004) 57–66.

[30] T.C. Ransohoff, C.J. Radke, Laminar flow of a wetting liquid along the corners of a predominantly gas-occupied noncircular pore, J. Colloid Interface Sci. 121 (2) (1988) 392–401.

[31] D. Zhou, M. Blunt, F.M. Orr, Hydrocarbon drainage along corners of noncircular capillaries, J. Colloid Interface Sci. 187 (1) (1997) 11–21.

[32] A. Al-Futaisi, T.W. Patzek, Three-phase hydraulic conductances in angular capillaries, SPE J. 8 (03) (2003) 252–261.

[33] OpenFOAM, The open source CFD toolbox. <http://www.openfoam.com>, 2016.

[34] R.I. Issa, Solution of the implicitly discretised fluid flow equations by operator-splitting, J. Comput. Phys. 62 (1) (1986) 40–65.

[35] L. Onsager, Reciprocal relations in irreversible processes. I., Phys. Rev. 37 (4) (1931) 405.

[36] M.C. Wendl, General solution for the Couette flow profile, Phys. Rev. E 60 (5) (1999) 6192.